Post-Print

This is the accepted version of:

M. Morelli, T. Bellosta, A. Guardone
Efficient Radial Basis Function Mesh Deformation Methods for Aircraft Icing
Journal of Computational and Applied Mathematics, Vol. 392, 2021, 113492 (18 pages)
doi:10.1016/j.cam.2021.113492

The final publication is available at https://doi.org/10.1016/j.cam.2021.113492

Efficient Radial Basis Function Mesh Deformation Methods for Aircraft Icing

Myles Morelli[a,b,*], Tommaso Bellosta[a], Alberto Guardone[a]

[a] *Department of Aerospace Science and Technology, Politecnico di Milano, Italy*
[b] *CFD Laboratory, School of Engineering, University of Glasgow, United Kingdom*

Abstract

This paper presents an approach to update the moving ice boundary resulting from aircraft icing simulations using radial basis function mesh deformation techniques. State-of-the-art surface and volume point reduction schemes are used to reduce the computational cost of the mesh deformation. The data reduction schemes which are utilized include multi-level greedy surface point selection and volume point reduction. The multi-level greedy surface point selection reduces the number of control points to increase the efficiency of the interpolation operation. While the volume point reduction improves the computational cost of the volume mesh update operation which is important for large data sets. The paper assesses the capabilities of radial basis function mesh deformation for both two and three-dimensional problems. Furthermore, the effectiveness of the deformation technique is assessed for both local, non-smooth deformations and global, smooth deformations. The convergence history of the multi-level greedy point selection is assessed in terms of number of control points and computational cost. The location of the selected control points near the ice accretion illustrates the efficacy of the method for localised deformations. The results show that the radial basis function mesh deformation performs well for both the two and three-dimensional problems. The data-reduction schemes utilized in this work represent a significant improvement to standard radial basis function mesh deformation for aircraft icing problems comprising of large data-sets

*Corresponding author, email address: mylescarlo.morelli@polimi.it

Preprint submitted to Journal of Computational and Applied Mathematics, February 28, 2021

typical of three-dimensional problems.

Keywords: Radial Basis Function, Mesh Deformation, Aircraft Icing

---

Nomenclature

List of Symbols

b	semi-span
c	chord
D	support distance of the wall distance function
$\mathbf{E}$	error vector of surface displacements
$f(\mathbf{r})$	function to be evaluated at position $\mathbf{r}$
k	volume reduction factor
N	number of points
$\mathbf{r}$	radial distance
R	support radius of the radial basis function
ΔS	surface displacement
ΔV	volume displacement
$\Delta\mathbf{X}$	x-displacement vector of mesh coordinates
$\Delta\mathbf{Y}$	y-displacement vector of mesh coordinates
$\Delta\mathbf{Z}$	z-displacement vector of mesh coordinates
α	weight coefficients of the basis points
ε	greedy tolerance
ξ	$d(\mathbf{r})/D$
ϕ	radial basis function
Φ	universal basis matrix
ψ	wall distance function

List of Subscripts

c	control points
l	multi-level
s	surface points
v	volume points

1. Introduction

In-flight icing encounters can jeopardise the performance and handling qualities of aircraft constituting to a serious threat to flight safety [1]. Ice accretion rapidly alters the geometric profile of aerodynamic lifting surfaces such as wings and rotors during flight. The ability to use computational techniques to simulate in-flight ice accretion has introduced an alternative approach to costly in-flight icing trials and experimental wind tunnel tests. As a consequence, it is helping to further understand this safety-critical issue. However, the simulation of in-flight icing using computational techniques is not without its own set of challenges. With the need to move towards fully three-dimensional in-flight icing simulations comes the issue of accounting for the moving ice boundary in the computational domain. Ice accretion can produce geometrically complex shapes and with numerical simulations being highly sensitive to the mesh quality, suitable mesh deformation schemes are required to maintain mesh orthogonality.

Well established techniques for mesh deformation such as the spring analogy [2, 3], the linear elasticity analogy [4, 5] and the interpolation method based on radial basis functions [6, 7, 8, 9] have been principally developed for moving boundary problem present in simulations such as fluid-structure interaction problems and aerodynamic shape optimization. The spring analogy, first developed by Batina [2], is one of the most widely used methods and models each edge of the mesh as a linear spring connected together at corresponding nodes. Significantly, Farhat et al. [3] further developed the spring analogy and introduced torsional stiffness to alleviate the mesh crossover problem. A concern with the

spring analogy is that it is expensive to solve and cannot guarantee high mesh quality during large deformations. The linear elasticity analogy extends from the spring analogy and models each mesh element as an elastic solid. The linear elasticity analogy has very high mesh quality during large mesh deformations however this comes at the expense of an increase in the CPU cost.

Boer et al. first applied radial basis function interpolation to mesh deformation [6]. Radial basis functions mesh deformations techniques have the unique property that they do not require the grid connectivity meaning that even for three-dimensional problems they are relatively simple to implement. Their work observed the superior mesh quality of radial basis function interpolation when compared to the spring analogy [6]. Rendall and Allen [8] then went on to show that radial basis function methods are robust and preserve high-quality mesh even during large deformations. One of the biggest deterrents to the radial basis function method, however, is that it is expensive for large scale problems when the number of surface points to be displaced becomes high. To address this issue and Rendall and Allen introduced data reduction schemes based upon greedy point selection algorithms to improve the efficiency of the interpolation operation [7, 10]. As a further enhancement, Wang et al. [11] introduced the concept of a multi-level subspace radial basis function interpolation method. To improve the volume update procedure Xie et al. [12] developed a volume reduction scheme for large data sets. It is clear from the expedited literature that radial basis function mesh deformation is becoming increasingly appealing as the CPU expense reduces with the latest data reduction schemes.

Mesh deformations occurring due to shape optimisation or the effects of wing or airframe elasticity results in possibly large but smooth displacements. Deformations due to aircraft icing are usually local in nature and can be characterised by non-smooth deformations. Consequently, accounting for the moving iced boundary using conventional mesh deformation techniques is challenging and is highlighted within the literature as being an issue [13].

This work seeks to explore how radial basis functions can be used with their robust mesh deformation properties for computational aircraft icing simulations

during the mesh update procedure. Groth et al. [14] first demonstrated the use of standard radial basis function mesh deformation techniques for icing simulations. Their work highlights the promise and potential of radial basis functions. However, significantly what it did not highlight was the critical issue of the costly nature of radial basis functions. The computational cost of radial basis function mesh deformation is one of the main disadvantages of the method and needs addressing if it is to be used in future aircraft icing simulations. Within this work the most concurrent data reduction schemes are utilized to efficiently update the moving iced boundary. These methods are implemented within the open-source SU2 code [15]. The ice accretion simulations are performed using the in-flight icing software suite PoliMIce developed by Politecnico di Milano [16].

An outline of the remaining paper follows: An introduction to radial basis functions and their use for mesh deformation is discussed in Section 2; The multi-level subspace data reduction schemes used in this work are described in Section 3; The volume reduction method for large data sets is discussed in Section 4; The results f both two- and three-dimensional problems are presented in Section 5; The main talking points from this study are discussed in Section 6;

2. Radial Basis Function Mesh Deformation

The term radial basis function refers to a series of functions whose values depends on their distance to a supporting position. In the most general of forms, radial basis functions can be written as, $\phi(\mathbf{r}, \mathbf{r}_i) = \phi\left(\|\mathbf{r} - \mathbf{r}_i\|\right)$, where the distance corresponds to the radial basis centre, $\mathbf{r}_i$. This distance is frequently taken as the Euclidean distance, meaning it becomes the spatial distance between two nodes. An interpolation function, $f(\mathbf{r})$ can then be introduced as a method for describing the displacement of a set of nodes in space and can be approximated by a weighted sum of basis functions. However, the interpolation relies on the weight coefficients of the basis points, α. The interpolation introduced

by Ref. [8] will now be discussed and takes the form

$$f(\mathbf{r}) = \sum_{i=1}^{N} \alpha_i \phi \left(\|\mathbf{r} - \mathbf{r}_i\| \right). \tag{1}$$

The weight coefficients of the basis points described in equation (1) can be obtained through the exact recovery of the known function values at the surface nodes. A prerequisite to this is knowing the surface node displacements a priori, however, this is typically the case for aircraft icing simulations so is not an issue. The displacement of the surface points are contained within the vector, $\Delta\mathbf{X}$ as described by

$$\Delta\mathbf{X}_s = \left[\Delta x_{s_1},\, \Delta x_{s_2},\, \ldots,\, \Delta x_{N_s} \right]^T , \tag{2}$$

where the subscript s denotes the surface points. This expression is reduced for the total number of surface points, N_s. The displacement in all x, y and z directions can be simplified to

$$\Delta S = \Delta\mathbf{X}_s \hat{\mathbf{x}} + \Delta\mathbf{Y}_s \hat{\mathbf{y}} + \Delta\mathbf{Z}_s \hat{\mathbf{z}} .$$

Similarly to the surface node displacements, the weight coefficients, $\boldsymbol{\alpha}$, can be contained within a vector

$$\boldsymbol{\alpha}_x = \left[\alpha_{x,s_1},\, \alpha_{x,s_2},\, \ldots,\, \alpha_{x,N_s} \right]^T .$$

For conciseness only the x components of the coefficients are shown, however, the y and z components are analogous. The universal basis matrix, $\boldsymbol{\Phi}$ can be constructed from the radial basis functions at each of the surface nodes and is consequently of the size of N_s^2. The universal basis matrix can then be shown in its compact form as

$$\boldsymbol{\Phi}_{s_j,\, s_i} = \phi \left\| r_{s_i} - r_{s_j} \right\| . \tag{3}$$

The coefficients can then be found by solving the following linear system

$$\boldsymbol{\Phi}_{s,s} \boldsymbol{\alpha} = \Delta S , \tag{4}$$

the volume displacements, ΔV, can finally be interpolated through the multiplication of the weight coefficients from equation (4) and the newly formed volume

node basis matrix, $\mathbf{\Phi}_{v,s}$, now of the size $N_v \times N_s$, as described by

$$\Delta V = \mathbf{\Phi}_{v,s}\boldsymbol{\alpha}\,, \tag{5}$$

where the subscript v represents the of volume points.

Multiple forms of radial basis functions exist within the literature which can be used for interpolating data sets and can be characterised into functions with global, local and, compact support. Functions with global support are always non-zero and grow with increasing distance from the radial basis function centre. Likewise, functions with local support are also always non-zero however decay with increasing distance from the radial basis function centre. Compact functions differ from global and local functions in that they decay to zero with increasing distance from the radial basis function centre. The choice of basis function is significant; global and local functions cover the entire interpolation space, leading to dense matrix systems which requires solving the linear system of a fully populated and ill-conditioned matrix. Compact functions are limited to a given support radius, R, resulting in sparse matrix systems which can be solved more easily however this sacrifices interpolation accuracy.

With practical application in mind, functions with compact support were considered within this work such that, $\phi\left(\|\mathbf{r}-\mathbf{r}_i\|/R\right)$. The Wendland compact radial basis functions [17] are shown in Table 1, where, $\eta = \left(\|\mathbf{r}-\mathbf{r}_i\|/R\right)$. The lower-order basis functions reduce the interpolation accuracy while the higher-order basis functions require a greater CPU cost. Considering this, the Wendland C2 basis function was chosen due to it providing improved smoothness in comparison to the C0 function and due to it being more efficient than the C4 and C6 functions and takes the form of

$$\phi(\eta) = \begin{cases} (1-\eta)^4\,(4\eta+1) & 0 \leq \eta < 1 \\ 0 & \eta \geq 1 \end{cases}\,. \tag{6}$$

3. Multi-Level Greedy Surface Point Selection

The high-quality mesh deformation properties of radial basis functions make them appealing, however, their relatively high CPU cost may prevent their use

Table 1: Wendland radial basis functions with compact support where, $\eta = (\|\mathbf{r} - \mathbf{r}_i\| / R)$.

Name	Basis Function
Wendland C0	$\phi(\eta) = (1-\eta)^2$
Wendland C2	$\phi(\eta) = (1-\eta)^4 (4\eta + 1)$
Wendland C4	$\phi(\eta) = (1-\eta)^6 (\frac{35}{3}\eta^2 + 6\eta + 1)$
Wendland C6	$\phi(\eta) = (1-\eta)^8 (32\eta^3 + 25\eta^2 + 8\eta + 1)$

on larger-scale problems where the number of surface points can frequently exceed 10^5. As introduced in equations (4) & (5), the size of the surface and volume basis matrices are N_s^2 and $N_s \times N_v$ respectively. The relative CPU cost associated with solving the linear algebra in equation 4 thus scales with N_s^3 while the CPU cost of interpolating equation (5) scales with $N_s \times N_v$. Methods throughout the literature have identified the size of N_s as being an issue for the solving of equation (4) and the interpolation of equation (5). Notably, Rendall and Allen published a method for reducing the number of surface points based on a greedy algorithm [10]. Their method starts with an initial control point and sequentially uses radial basis function interpolation to find the subsequent control point with the largest error signal. The process repeats itself until the surface interpolation meets a desired tolerance. The implementation of this greedy point selection will now be introduced.

An initial control point is first selected and added to the control points vector, $\mathbf{X}_c$. The choice of the first control point is arbitrary thus, the first point on the list of surface nodes is used, $\mathbf{X}_s^{(0)}$. Such that

$$\mathbf{X}_c = \mathbf{X}_s^{(0)},$$

where the subscript c denotes the control points and the subscript s represents the surface points. The size of the control points vector is of the size N_c, and since this is the first iteration of the greedy selection process $\mathbf{X}_c$ contains only a singular element.

An error signal is then used to guide the greedy algorithm when selecting

control points. Within this work an error vector, $\mathbf{E}$, based on the difference between actual surface displacements and computed surface displacements is used

$$\mathbf{E} = \Delta S - \mathbf{\Phi}_{s,c}\boldsymbol{\alpha}\,, \tag{7}$$

with the basis matrix, $\mathbf{\Phi}_{s,\,c}$, now being of the size of $N_s \times N_c$ and where $\mathbf{E}$ is of the size of N_s. The element of the error vector with the largest error signal, $\mathbf{E}^{(\max)}$, is then used to identify the subsequent control point to be added to $\mathbf{X}_c$. This greedy selection process continues until the largest error signal normalized by ΔS meets a desired tolerance, ε, as described by

$$\frac{\mathbf{E}^{(\max)}}{\Delta S} < \varepsilon\,.$$

The size of $\mathbf{X}_c$ therefore depends on the number of iterations of the greedy selection process.

The greedy point selection thus allows for the reduction in the number of points being used for solving the linear algebra in equation (4) and for the interpolation in equation (5), however, the greedy system itself requires significant outlay as every time a control point is added to the system the coefficients need to be solved once more. This therefore means that the CPU cost associated with solving the greedy selection process becomes of the order of N_c^4. Wang et al. addressed this issue by introducing a multi-level subspace radial basis function interpolation where, at the end of each level, the error of that interpolation step is used as the object for the subsequent interpolation step [11] and can be expressed as

$$\Delta S_{l+1} = \mathbf{E}\,,$$

where the subscript "$l+1$" denotes the next level of the multi-level greedy selection process. The new error is then computed based on the residual from the previous step and with $\Delta S_{l+1} \ll \Delta S_l$ the size of the displacements is reduced significantly. The error signal described by equation (7) is consequently updated and becomes

$$\Delta S_{l+1} = \Delta S_l - \mathbf{\Phi}_{s,c}\boldsymbol{\alpha}\,.$$

The number of subspace levels, N_l, is used to continuously reduce the error which allows the multi-level greedy method to be more efficient than the single-level greedy method. The multi-level greedy selection process can be summarised as follows

$$\Delta S = \sum_{i=0}^{i=N_l-1} \Delta S^{(i)} = \sum_{i=0}^{i=N_l-1} \mathbf{\Phi}_{s,c}^{(i)} \boldsymbol{\alpha}^{(i)} \quad , \tag{8}$$

$$\Delta V = \sum_{i=0}^{i=N_l-1} \Delta V^{(i)} = \sum_{i=0}^{i=N_l-1} \mathbf{\Phi}_{v,c}^{(i)} \boldsymbol{\alpha}^{(i)} \quad . \tag{9}$$

4. Volume Point Reduction

The reduced number of control points after the multi-level greedy point selection now means that the CPU cost of interpolating equation 5 scales with $N_l \times N_c \times N_v$. To efficiently obtain the volume point displacements, it is thus of interest to reduce N_v for large-scale problems since it can often be in the order of magnitude of $N_s \times \sqrt{N_s}$. A wall distance-based function, ψ, is therefore introduced to restrict the N_v based on the work from Xie and Liu [12], namely

$$\psi = \psi \left(\frac{d(\mathbf{r})}{D} \right) ,$$

where $d(\mathbf{r})$ signifies the wall distance and D is the support distance of the wall function. The wall distance function is of compact support, which means it decays and is zero outwith the support distance as shown,

$$\psi(\xi) = \begin{cases} (1-\xi) & 0 \leq \xi < 1 \\ 0 & \xi \geq 1 \end{cases} ,$$

where $\xi = d(\mathbf{r})/D$ is the wall distance normalised by the support distance. The distance D is computed as a function of the maximum surface displacement and by using a volume reduction factor, k. Accordingly, distance D, can be expressed as

$$D = k(\Delta S_l)^{max} .$$

The wall distance function is then included in the interpolation function, $f(\mathbf{r})$, in equation (1) and the updated function has the form

$$f(\mathbf{r}) = \psi\left(\frac{d(\mathbf{r})}{D}\right)\sum_{i=1}^{N}\alpha_i\phi\left(\|\mathbf{r}-\mathbf{r}_i\|\right) . \tag{10}$$

Updating the support distance after each level is possible since $\Delta S_{l+1} \ll \Delta S_l$, meaning the number of volume points in the sphere of influence of the basis function is less. Therefore $D_{l+1} \ll D_l$ and so the number of updated volume points $N_{v,l+1} \ll N_{v,l}$ helping to reduce the cost of the interpolation step.

5. Results

In order to assess radial basis function mesh deformation techniques for aircraft icing two test cases are evaluated. The first test case is conducted on a two-dimensional airfoil and the second test case is conducted on a three-dimensional swept-wing. The performance of the data-reduction schemes and robustness of the deformation in terms of the mesh quality are evaluated. Additionally, the non-smooth ice deformations are compared to well-known benchmark test cases for radial basis function mesh deformation with smooth deformations. Finally there is a comparison of the radial basis function mesh deformation technique with the standard linear-elasticity approach. All simulations are run on a single processor to focus on the efficiency of the mesh deformation techniques opposed to the scalability and parallelism of the code. The processor used was an Intel(R) Xeon(R) X5660 CPU with a clock speed of 2.80GHz.

5.1. 2D – NACA0012 Airfoil

The aim of the first test case is to assess the efficiency and robustness of radial basis function mesh deformation data-reduction schemes on a two-dimensional icing problem. Experimental icing tests on a NACA0012 airfoil performed in the NASA Lewis Icing Research Tunnel (IRT) [18] are used as a reference for the numerical icing predictions. One subset of these conditions is chosen and is outlined in Table 2.

Table 2: NACA0012 icing conditions.

Airfoil	Time	AoA	Chord	Pressure	Airspeed	OAT	LWC	MVD
[-]	[s]	[°]	[m]	[Pa]	[m/s]	[K]	[g/m^3]	[μm]
NACA0012	120	0	0.3	90,700	129	260.55	0.5	20

The spatial discretization of the two-dimensional airfoil mesh is achieved using a structured multi-block grid and is shown in Fig. 1. The total number of elements in the domain is 44 055 and the total number of vertices is 44 500. The NACA0012 airfoil has 247 vertices distributed around its surface with vertices congregated around the leading and trailing edges. The far-field is placed 25 chord lengths from the airfoil. The grid resolution is sufficient at the wall to ensure $y^+ < 1$.

The SU2 solver [15] is used to determine the flow field by solving the RANS equations. The standard one-equation SA turbulence model is used for closure of the RANS equations. The convective fluxes are computed using the Roe scheme and second-order accuracy is achieved using the MUSCL scheme. The viscous fluxes are approximated using the weighted-least-squares numerical method. The flow solution is considered converged when there is a reduction of 6 orders of magnitude on the density residual.

The PoliMIce software library provides state-of-the-art ice formation models [16]. The model used in this work to capture the complex experimental ice shapes is the local exact solution of the unsteady Stefan problem for the temperature profiles within the ice layer in glaze conditions [19]. Multi-step ice accretion simulations are performed at 5 second intervals to update the solution and account for unsteady ice accretion. The final predicted ice shape after 120 seconds of ice accretion is compared against the measured data from Ref. [18] and is shown in Fig. 2. The ice shape exhibits distinct horns paradigmatic of the glaze ice regime and the overall mass of ice is in agreement with the experimental measurements.

The compactly supported Wendland C2 function is used to deform the iced

mesh. Points within the support radius of $R = 2c$ are deformed. Altogether five levels of multi-level greedy surface point reduction are used. Each level is updated when there is a reduction of $\varepsilon = 10^{-1}$ in the normalized error. A volume reduction factor of $k = 5$ is chosen.

The non-smooth, local deformations caused by ice accretion are compared to a benchmark test case taken from Ref. [12] with global, smooth deformations. The benchmark test case imposes a sinusoidal motion to the airfoil which can be described by

$$\Delta y = 0.01 \sin(15\pi x) \ ,$$

where Δy describes the displacement of the airfoil as a function of its position in the x-direction along its chord, c. The sinusoidal motion thus represents a more globalised deformation of the airfoil. Identical radial basis function parameters are used to ensure maximum similarity between local and global deformations.

The results of the radial basis function deformation due to ice accretion and sinusoidal motion are summarised in Table 3. The main findings will now be discussed.

The convergence history of the normalized displacement error for both the iced and sinusoidal deformation are respectively illustrated in Figs. 3 & 4. The efficiency of the multi-level greedy point selection performs well in terms of maintaining a low number of control points and in terms of CPU time for both test cases. Both kinds of deformation achieve 5 levels of greedy surface point selection. The sinusoidal deformation shows marginally improved performance during the initial levels. However, at the highest level both kinds of deformation show similar performance. The iced deformation shown in Fig. 3 requires 179 control points at the 5^{th} level and has an associated CPU time of approximately 1.14 s. While the sinusoidal deformation shown in Fig. 4 requires 182 control points at the 5^{th} level and thus exhibits a similar CPU time of approximately 1.16 s.

The control points selected from the $1^{\text{st}} \rightarrow 4^{\text{th}}$ levels of the greedy process for both the iced and sinusoidal deformation are respectively shown in Figs. 5

Table 3: Influence of the kind of deformation on the performance of the multi-level greedy surface point selection scheme: local vs. global

Kind of Deformation	N_c	N_v	CPU time (s)	Min. Ortho.
Ice Accretion:				
Level-1	23	16 406	0.018	0.305
Level-2	48	10 502	0.078	0.308
Level-3	107	6199	0.383	0.353
Level-4	132	2727	0.591	0.355
Level-5	179	743	1.137	0.355
Sinusoidal:				
Level-1	11	18 347	0.032	0.370
Level-2	24	11 853	0.084	0.372
Level-3	49	6943	0.187	0.372
Level-4	110	3223	0.509	0.372
Level-5	182	743	1.158	0.372

& 6. The local ice deformation has control points which are predominately distributed around the leading edge of the airfoil as shown in Fig. 5. This leads to a highly anisotropic control point distribution. It is evident that for ice shapes with any kind of level of roughness or horns, a large number of control points are required otherwise the radial interpolation may potentially smooth over these local features. Contrarily, the global sinusoidal deformation has control points which are relatively evenly distributed as shown in Fig. 6. At the lower levels, the control points are selected at the peaks of the sinusoidal waves. As the greedy algorithm progresses, the control point list becomes more populated and control points are relatively evenly distributed along the airfoil.

The influence of the kind of deformation on the mesh quality is shown in Fig. 7. The mesh quality is evaluated by the orthogonality angle. The results show that a relatively high orthogonality angle is preserved throughout the simulations when compared to the clean mesh as shown in Fig. 7a. The localised ice deformation shown in Fig. 7b causes an isolated reduction in the mesh quality

Table 4: Influence of the deformation technique on the performance.

Deformation Technique	N_c	N_v	CPU time (s)	Min. Ortho.
RBF Standard	247	44500	2.731	0.355
RBF Multi-Level	179	743	2.207	0.355
Linear-Elasticity	247	44500	2.558	0.334

at the leading edge. While the global sinusoidal deformation shown in Fig. 7c causes a more universal reduction in the mesh quality with the greatest degradation located at the peaks of the sinusoidal waves.

To further assess the effectiveness of this technique for aircraft icing, it is compared to the more traditional linear elasticity analogy. For this two-dimensional test case, the elastic stiffness of each element is inversely proportional to the cell volume to help preserve the mesh quality within the boundary-layer. For completeness, the standard radial basis function technique is also compared. A summary of the results is described in Table 4 while the resultant mesh quality is shown in Fig. 8. The results show that both radial basis function mesh deformation techniques provide identical mesh orthogonality irrespective of the number of control points. Meanwhile, the linear-elasticity approach provides similar mesh orthogonality near the ice horns. The CPU time for each technique is comparable for this two-dimensional problem.

5.2. 3D – Swept Wing

The aim of the second test case is to assess the efficiency and robustness of radial basis function mesh deformation data-reduction schemes on a three-dimensional icing problem. Experimental icing tests on a swept-wing with a NACA0012 profile performed in the NASA Glenn Icing Research Tunnel (IRT) [20] are used. One subset of these conditions is chosen and is outlined in Table 5.

The spatial discretization is achieved using an unstructured mesh which is shown in Fig. 9. The total number of elements in the domain is 2 030 599 and the total number of vertices is 591 225. The swept wing has 21 650 vertices

Table 5: Swept-wing icing conditions.

Wing Profile	Sweep [°]	Time [min]	AoA [°]	Chord [m]	Airspeed [m/s]	OAT [K]	LWC [g/m^3]	MVD [μm]
NACA0012	45	19.8	0	0.914	51.44	260.55	0.57	44

distributed around its surface with there being an even distribution around the wing. The far-field is placed 20 chord lengths from the wing. The grid resolution is sufficient at the wall to ensure $y^+ < 1$.

The SU2 solver configuration settings used to determine the aerodynamic flow field of the two-dimensional case are also used for the three-dimensional swept-wing case. The same applies to the ice accretion simulation settings of PoliMIce. The final predicted ice shape after 19.8 minutes of ice accretion is shown in Fig. 10a. The ice shape exhibits a spearhead like shape paradigmatic of the rime regime along the leading edge of the wing.

The compactly supported Wendland C2 function is used to deform the iced mesh. Points within the support radius of $R = 3c$ are deformed. Three levels of multi-level greedy surface point reduction are used. Each level is updated when there is a reduction of $\varepsilon = 10^{-1}$ in the normalized error. A volume reduction factor of $k = 5$ is chosen.

The sinusoidal benchmark test case is extended to the three-dimensional swept-wing test case. Sinusoidal motion is applied to the swept-wing in the span-wise direction and can be described by

$$\Delta y = 0.03 \sin(4\pi z) \ , \tag{11}$$

where Δy describes the displacement of the swept-wing as a function of its position in the z-direction along its span, b. The deformation applied to the swept-wing is shown in Fig. 10b. Identical radial basis function parameters are again used to ensure maximum similarity between the localised iced deformation and the global sinusoidal deformation.

The three-dimensional results of the radial basis function deformation due

Table 6: Influence of the kind of deformation on the performance: local vs. global

Kind of Deformation	N_c	N_v	CPU time (s)	Min. Ortho.
Ice Accretion:				
Level-1	492	498 261	8.411	0.386
Level-2	2767	360 000	1072.064	0.398
Level-3	5214	260 321	10 087.194	0.399
Sinusoidal:				
Level-1	102	646 725	1.286	0.366
Level-2	395	579 973	16.762	0.367
Level-3	1297	205 057	256.408	0.372
Level-4	3437	90 457	4148.168	0.375

to ice accretion and sinusoidal motion are summarised in Table 6. The main findings will now be outlined.

The convergence history of the normalized displacement error for both the iced and sinusoidal deformation of the swept-wing are respectively illustrated in Figs. 11 & 12. Given the increase in size of the data-set, the efficiency of the multi-level greedy point selection performs well in terms of maintaining a low number of control points and in terms of CPU time. When comparing these two test cases it is clear that the global sinusoidal deformation performs better. While the localised iced deformation shown in Fig. 11 can obtain three-levels of greedy surface point selection, the global sinusoidal deformation shown in Fig. 12 can obtain four-levels of greedy surface point selection. In essence, while global sinusoidal deformations can be characterised by a small number of control points, localised iced deformations simply cannot. Despite this, satisfactory reduction in the normalised surface error is achieved by both test cases. Most significantly of all, the data-reduction techniques do indeed help to reduce the high CPU cost associated to radial basis function mesh deformation on large data-sets. Notably within the first 60 seconds of the iced and sinusoidal deformations, normalized surface errors of 10^{-3} and 10^{-4} are respectively achieved as revealed in Figs. 11b &12b.

The control points selected throughout the multi-level greedy selection process for both the iced and sinusoidal deformation are respectively shown in Figs. 13 &14. The test cases exhibit significantly different distributions of control points. The local iced deformation illustrated in Fig. 13 depicts the intelligence of the selection process to use control points primarily congregated around the leading edge of the swept-wing where ice is accreted. Resultantly an anisotropic control point distribution is present. The global sinusoidal deformation visible in Fig. 14 displays a more expansive distribution of selected control points around the swept-wing which reflects the deformation described by Eq. (11).

The influence of the kind deformation on the mesh quality is shown in Figs. 15 &16. The orthogonality angle of iced and sinusoidal deformed mesh is compared to that of the undeformed mesh. The first location of interest is in the $x - z$ plane at $y = 0$ and is shown in Fig. 15. This cut-plane provides a convenient view of the iced mesh. It shows there is a slight decrease in the mesh quality along the leading edge of the iced mesh. Despite this, the overall impact of the ice accretion on the mesh quality appears low. In this plane of view it is difficult to asses the impact of the sinusoidal deformation on the mesh quality. The second location of interest is in the $y - z$ plane at $x = c$ and is shown in Fig. 16. Likewise to the previous view, this exposes the marginal reduction in the mesh quality at the leading edge of the iced mesh. This cut-plane however provides a more favourable view of the sinusoidal deformation. Resultantly, it can be adjudged that the mesh quality of the sinusoidal deformation is also satisfactory.

To further evaluate the performance of this technique for three-dimensional aircraft icing problems, it is compared to the more standard linear elasticity analogy. The linear elasticity equations contain material properties which are related to the mesh characteristics and may be solved using different approaches. This three-dimensional test case considers three different approaches with the elastic stiffness being inversely proportional to the cell volume, the elastic stiffness being inversely proportional to the wall distance, and a constant elastic

Table 7: Influence of the deformation technique on the performance.

Deformation Technique	N_c	N_v	CPU time (s)	Min. Ortho.
RBF:				
Standard	21 650	2 030 599	275 684	0.399
Multi-Level (2)	2767	360 000	1072	0.398
Multi-Level (3)	5214	260 321	10 087	0.399
Linear-Elasticity:				
Inverse Volume	21 650	2 030 599	4080	−0.350
Wall Distance	21 650	2 030 599	4104	0.356
Constant Stiffness	21 650	2 030 599	4158	−0.898

stiffness with Poisson's ratio being equal to the aspect ratio of the element. Alongside this, the standard radial basis function mesh deformation technique is compared to the multi-level implementation. A summary of the results is described in Table 7 while the resultant mesh quality is shown in Fig. 17. The results show that all variants of the radial basis function techniques produce viable mesh. On the contrary, only the linear elasticity approach based on the inverse of the wall distance produces a viable mesh. The approach based on the inverse volume has negative volume elements towards the wing-tip while the approach based on the constant stiffness has negative volume elements within the boundary-layer. Additionally, it can be concluded that two levels of greedy surface point selection are sufficient to obtain a high-quality mesh at a fraction of the CPU cost of standard radial basis function techniques and the linear elasticity approach.

6. Conclusion

This work evaluates radial basis function mesh deformation techniques for their use within aircraft icing simulations. In this work state-of-the-art multi-level greedy surface point reduction and volume point reduction algorithms are used. The efficiency and robustness of the approach is illustrated using a two-

dimensional iced airfoil and three-dimensional swept-wing exposed to icing conditions. The data-reduction methods help to reduce the computational cost of the deformation process while maintaining a high mesh quality. The method allows for the isolation of control points where the ice is present. The convergence history of the airfoil test case performs well with limited control points required at each level and subsequently ensures high performance. The convergence history of the much larger swept-wing test case also performs well and is able to achieve three levels of greedy surface point selection. The introduction of these techniques to aircraft icing simulations provides a significant improvement to the efficiency of standard radial basis function mesh deformation and to the robustness of traditional mesh deformation techniques. Simultaneously, this work highlights the promise of radial basis function mesh deformation techniques and hopes to help provide a reasonable solution to the challenge that is accounting for the moving ice boundary.

Acknowledgments

The NITROS (Network for Innovative Training on ROtorcraft Safety) project has received funding from the European Union's Horizon 2020 research and innovation program under the Marie Skłodowska-Curie grant agreement No. 721920. The ICE GENESIS project has received funding from the European Union's Horizon 2020 research and innovation program under grant agreement No. 824310.

Figures

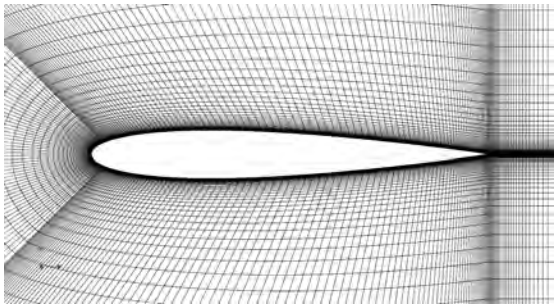

Figure 1: Structured NACA0012 airfoil mesh. Constructed using the multi-block grid strategy.

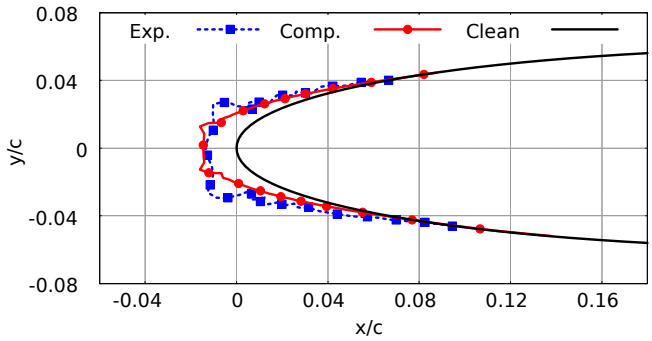

Figure 2: Comparison of computed and experimental ice shapes on a NACA0012 airfoil under conditions identified in Table 2.

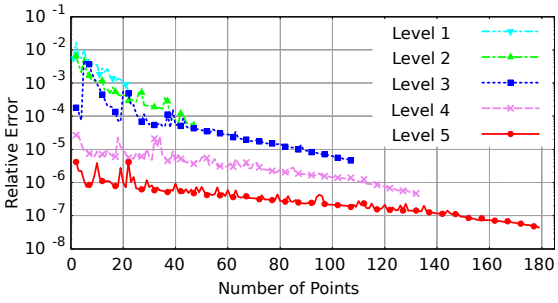

(a) Convergence history in terms of selected points.

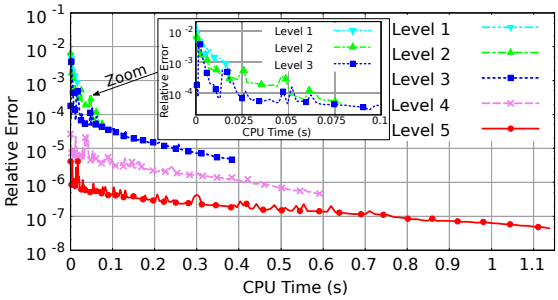

(b) Convergence history in terms of CPU time.

Figure 3: Comparison of error reduction rates in terms of selected points and CPU time for the NACA0012 airfoil.

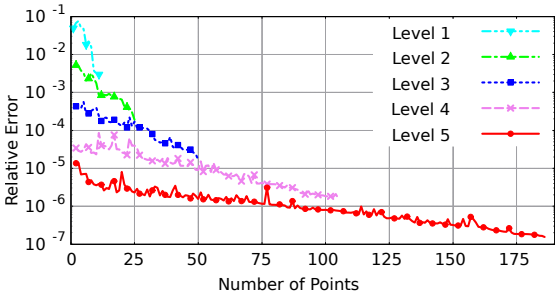

(a) Convergence history in terms of selected points.

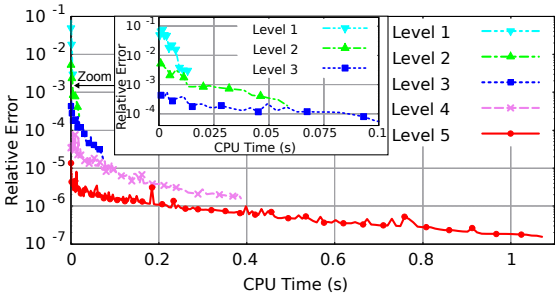

(b) Convergence history in terms of CPU time.

Figure 4: Comparison of error reduction rates in terms of selected points and CPU time for the NACA0012 airfoil with sinusoidal motion.

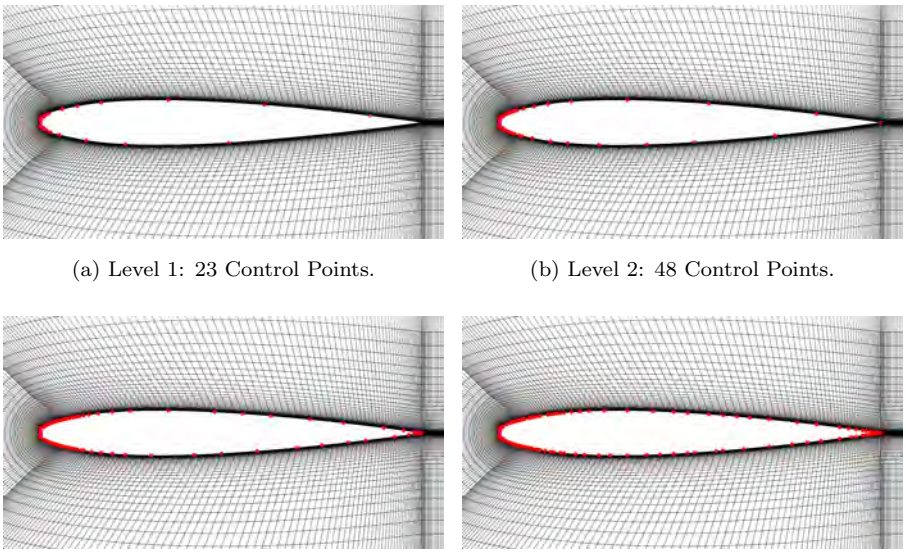

(a) Level 1: 23 Control Points.

(b) Level 2: 48 Control Points.

(c) Level 3: 107 Control Points.

(d) Level 4: 132 Control Points.

Figure 5: Control points selected during the multi-level greedy point selection for the NACA0012 airfoil; where the red points indicate the control points.

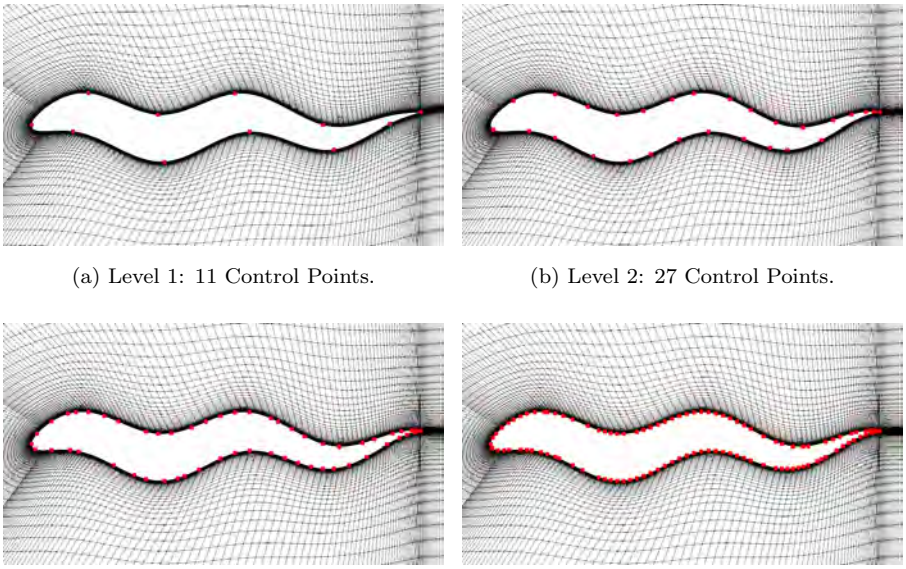

(a) Level 1: 11 Control Points.

(b) Level 2: 27 Control Points.

(c) Level 3: 53 Control Points.

(d) Level 4: 108 Control Points.

Figure 6: Control points selected during the multi-level greedy point selection for the airfoil with sinusoidal motion; where the red points indicate the control points.

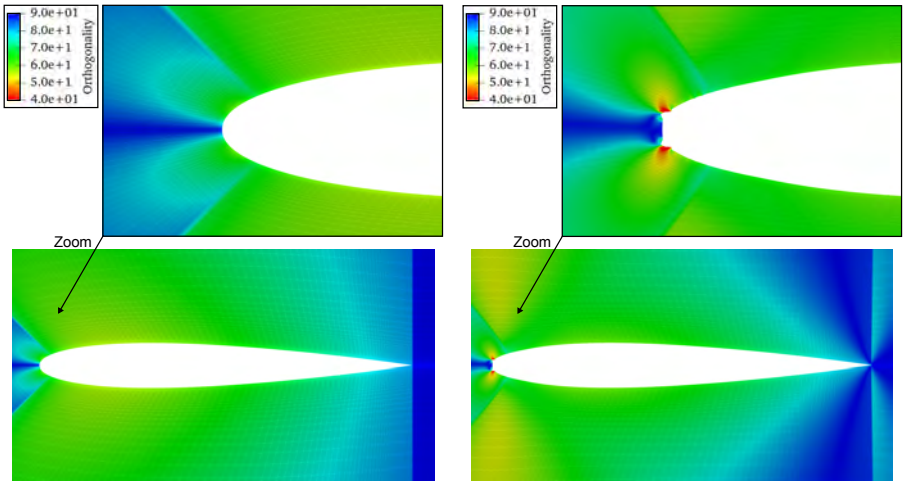

(a) Orthogonality of the clean airfoil mesh prior to deformation.

(b) Orthogonality of the iced airfoil mesh post deformation.

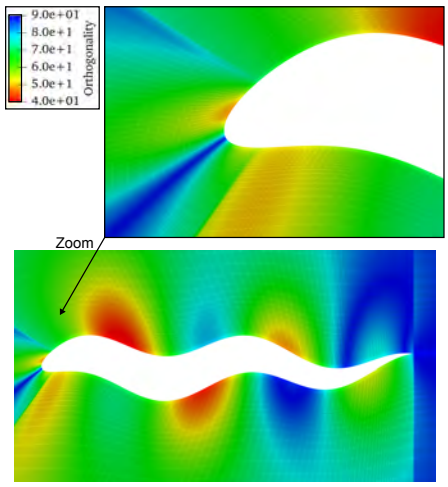

(c) Orthogonality of the sinusoidal airfoil mesh post deformation.

Figure 7: Influence of the kind of deformation on the mesh quality. Comparing localised deformation to global deformation.

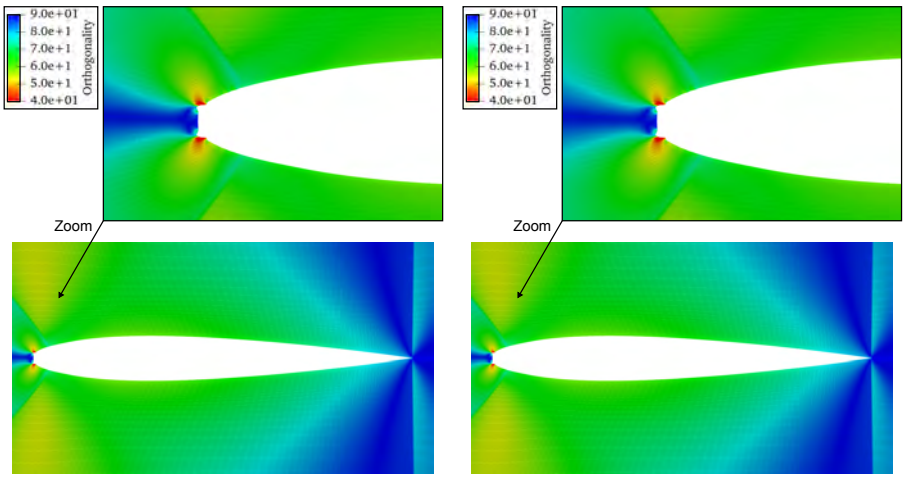

(a) Standard RBF approach.

(b) Multi-level RBF approach.

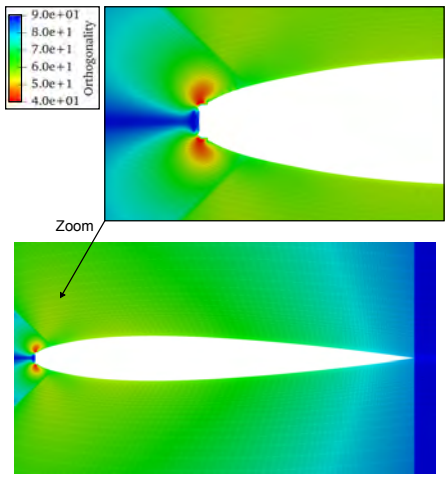

(c) Linear-elasticity approach.

Figure 8: Influence of the deformation technique on the mesh quality. Comparing the standard RBF, multi-level RBF, and linear-elasticity approaches.

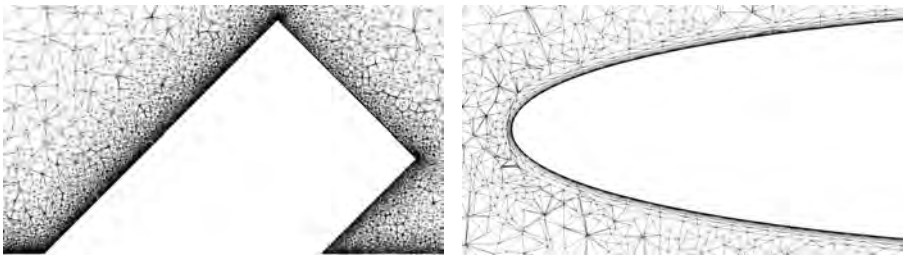

(a) Unstructured volume mesh in the $x-z$ cut-plane at $y = 0$.

(b) Close-up view of the leading edge volume mesh in the $x - y$ cut-plane at $z = 0.5b$.

Figure 9: Unstructured swept wing mesh. Constructed using a NACA0012 airfoil and based on a 45° sweep angle.

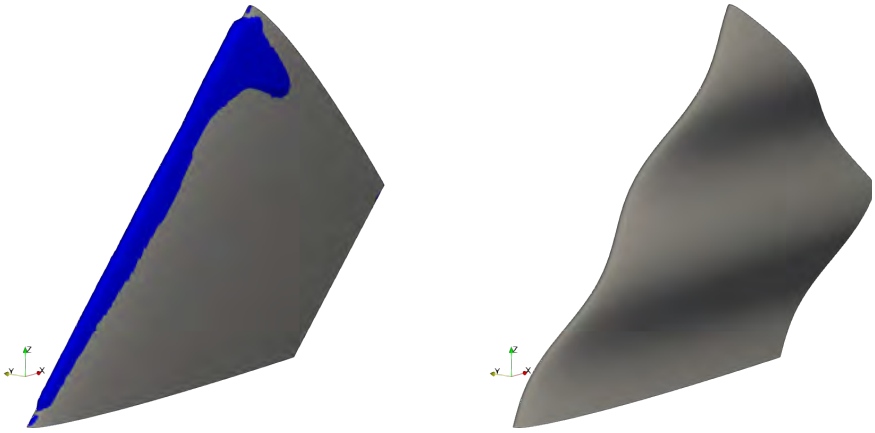

(a) Predicted ice shape under the conditions identified in Table 5.

(b) Sinusoidal motion of the wing described by Eq. 11.

Figure 10: Different kinds of deformation applied to the swept wing. Firstly, the ice shape which is displayed in blue and depicts a non-smooth, local deformation. Secondly, the sinusoidal motion which represents a smooth, global deformation.

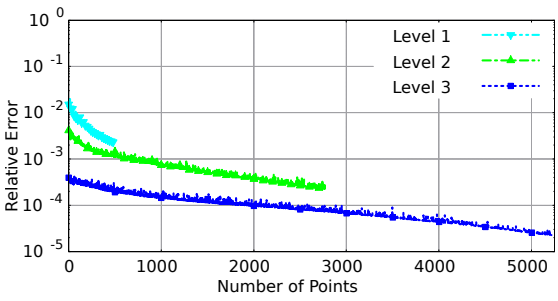

(a) Convergence history in terms of selected points.

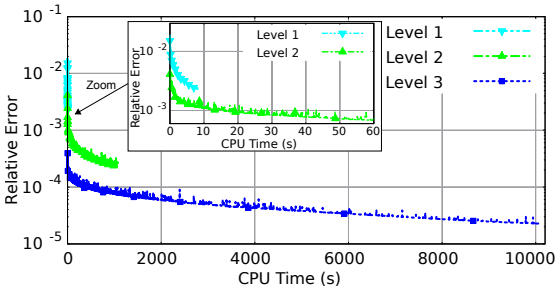

(b) Convergence history in terms of CPU time.

Figure 11: Comparison of error reduction rates in terms of selected points and CPU time for the NACA0012 swept wing post deformation due to icing.

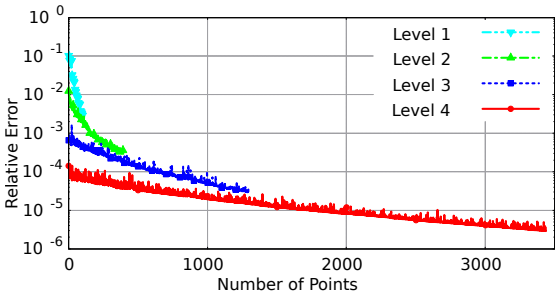

(a) Convergence history in terms of selected points.

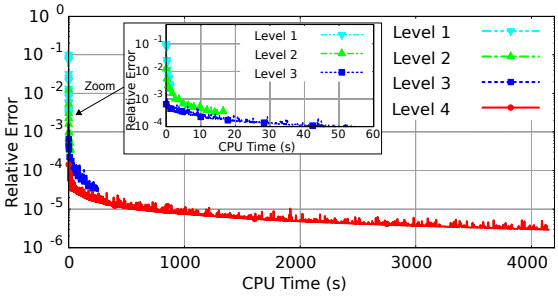

(b) Convergence history in terms of CPU time.

Figure 12: Comparison of error reduction rates in terms of selected points and CPU time for the NACA0012 swept wing post deformation due to sinusoidal motion.

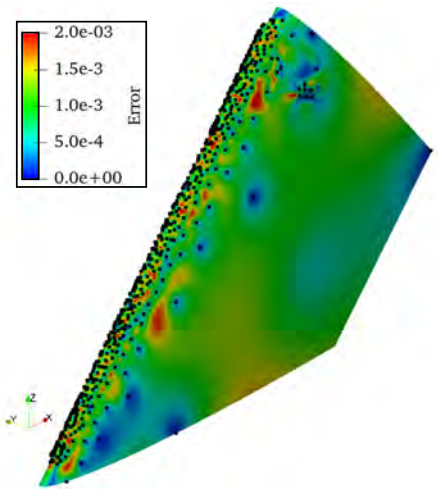

(a) Level 1: 492 Control Points.

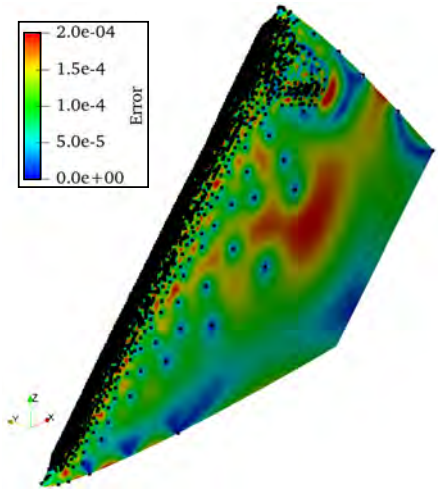

(b) Level 2: 2767 Control Points.

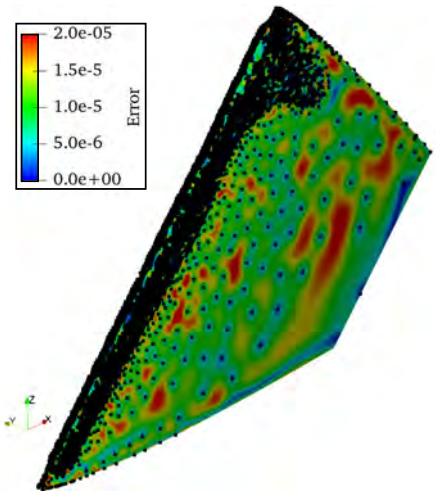

(c) Level 3: 5214 Control Points.

Figure 13: Contour map of the normalized surface error during the multi-level greedy point selection on the iced wing. The black points indicate the control points.

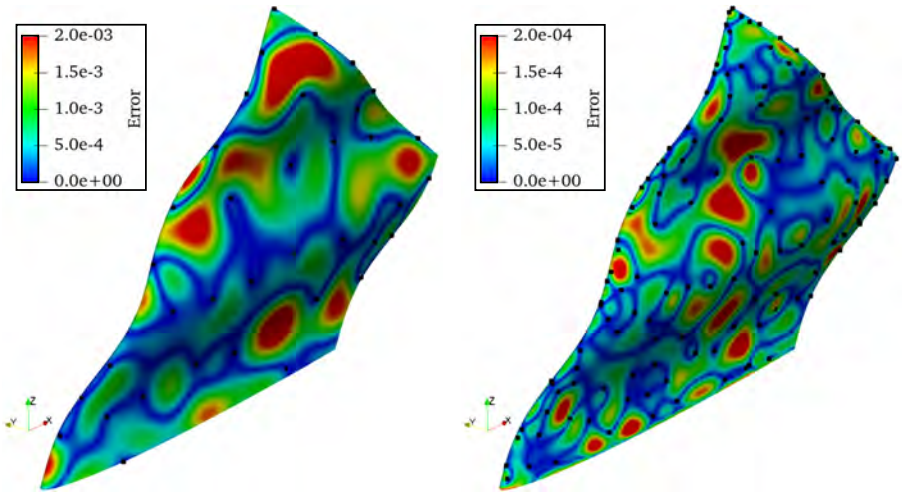

(a) Level 1: 102 Control Points.

(b) Level 2: 395 Control Points.

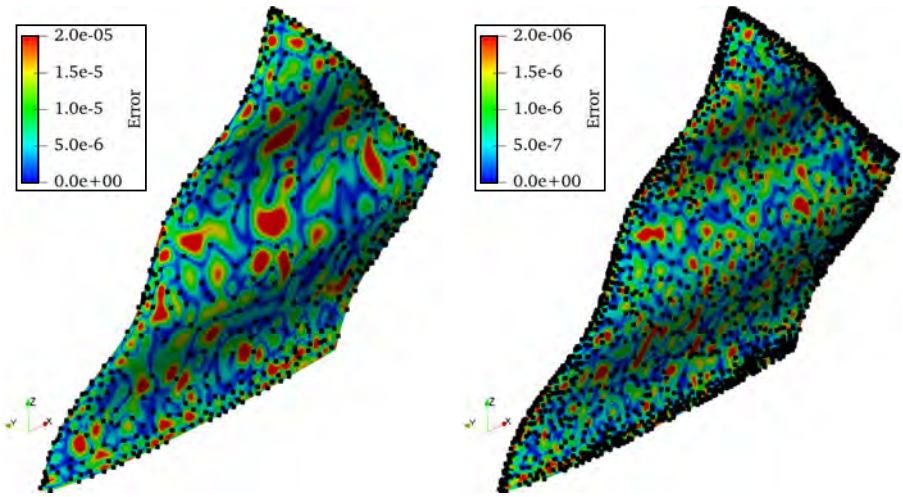

(c) Level 3: 1297 Control Points.

(d) Level 4: 3437 Control Points.

Figure 14: Contour map of the normalized surface error during the multi-level greedy point selection on the sinusoidal. The black points indicate the control points.

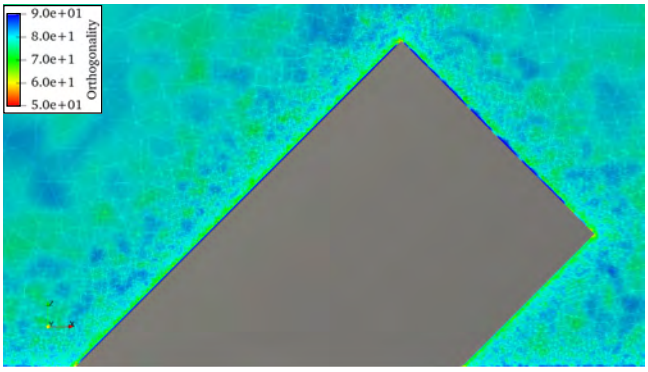

(a) Orthogonality of the clean wing mesh prior to deformation.

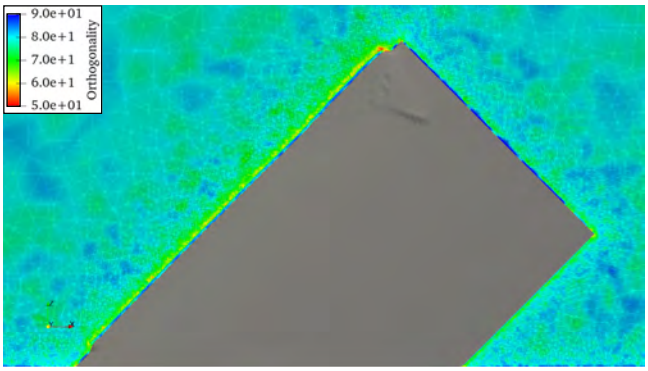

(b) Orthogonality of the iced wing mesh post deformation.

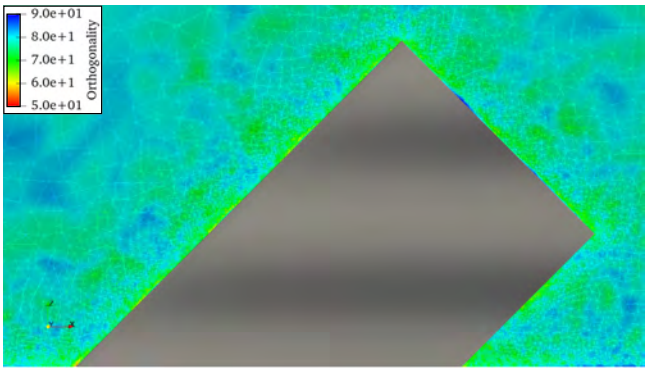

(c) Orthogonality of the wing mesh post sinusoidal deformation.

Figure 15: Influence of the kind of mesh deformation on the quality of the swept wing mesh in the $x - z$ plane at $y = 0$.

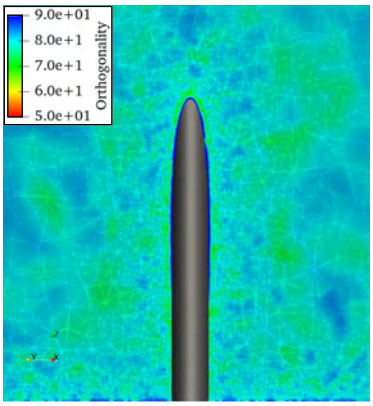

(a) Orthogonality of the clean wing mesh prior to deformation.

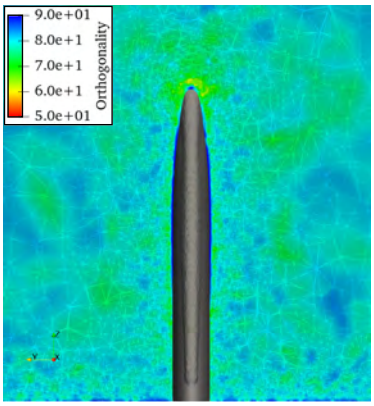

(b) Orthogonality of the iced wing mesh post deformation.

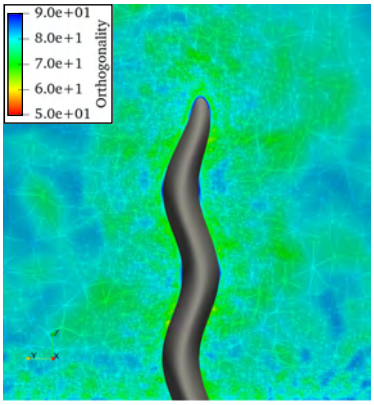

(c) Orthogonality of the wing mesh post sinusoidal deformation.

Figure 16: Influence of the kind of mesh deformation on the quality of the swept wing mesh in the $y - z$ plane at $x = c$.

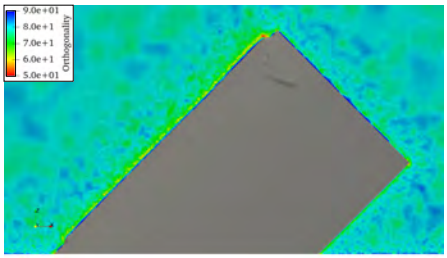

(a) RBF: 2 levels of greedy selection.

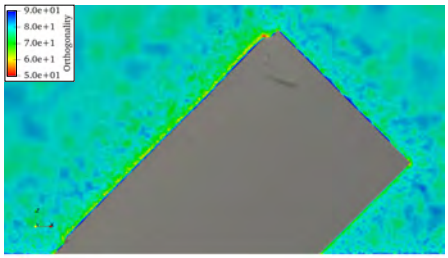

(b) RBF: 3 levels of greedy selection.

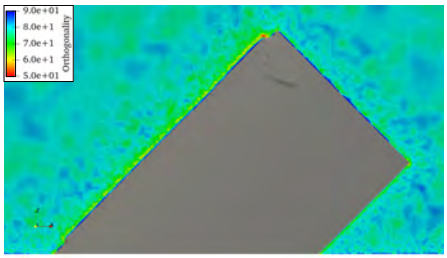

(c) Standard RBF.

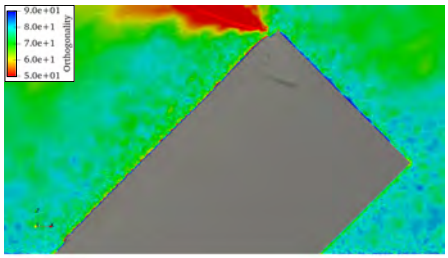

(d) Linear-elasticity: inverse volume.

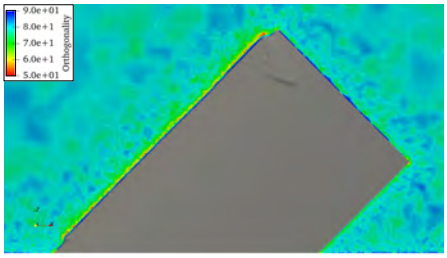

(e) Linear-elasticity: wall distance.

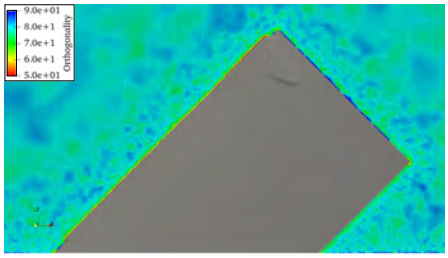

(f) Linear-elasticity: constant stiffness.

Figure 17: Influence of the kind of deformation technique on the mesh quality of the swept wing mesh in the $x - z$ plane at $y = 0$.

References

[1] R. Gent, N. Dart, J. Cansdale, Aircraft icing, Philosophical Transactions of the Royal Society of London. Series A: Mathematical, Physical and Engineering Sciences 358 (1776) (2000) 2873–2911, https://doi.org/10.1098/rsta.2000.0689.

[2] J. T. Batina, Unsteady euler airfoil solutions using unstructured dynamic meshes, AIAA journal 28 (8) (1990) 1381–1388, https://doi.org/10.2514/3.25229.

[3] C. Farhat, C. Degand, B. Koobus, M. Lesoinne, Torsional springs for two-dimensional dynamic unstructured fluid meshes, Computer methods in applied mechanics and engineering 163 (1-4) (1998) 231–245, https://doi.org/10.1016/S0045-7825(98)00016-4.

[4] T. Baker, P. Cavallo, Dynamic adaptation for deforming tetrahedral meshes, in: 14th Computational Fluid Dynamics Conference, Norfolk, Virginia, U.S.A, 01-05 November, 1999, p. 3253, https://doi.org/10.2514/6.1999-3253.

[5] E. J. Nielsen, W. K. Anderson, Recent improvements in aerodynamic design optimization on unstructured meshes, AIAA journal 40 (6) (2002) 1155–1163, https://doi.org/10.2514/2.1765.

[6] A. De Boer, M. Van der Schoot, H. Bijl, Mesh deformation based on radial basis function interpolation, Computers & structures 85 (11-14) (2007) 784–795, https://doi.org/10.1016/j.compstruc.2007.01.013.

[7] T. C. Rendall, C. B. Allen, Efficient mesh motion using radial basis functions with data reduction algorithms, Journal of Computational Physics 228 (17) (2009) 6231–6249, https://doi.org/10.1016/j.jcp.2009.05.013.

[8] T. C. Rendall, C. B. Allen, Unified fluid–structure interpolation and mesh motion using radial basis functions, International jour-

nal for numerical methods in engineering 74 (10) (2008) 1519–1559, https://doi.org/10.1002/nme.2219.

[9] A. Beckert, H. Wendland, Multivariate interpolation for fluid-structure-interaction problems using radial basis functions, Aerospace Science and Technology 5 (2) (2001) 125–134, https://doi.org/10.1016/S1270-9638(00)01087-7.

[10] T. C. Rendall, C. B. Allen, Reduced surface point selection options for efficient mesh deformation using radial basis functions, Journal of Computational Physics 229 (8) (2010) 2810–2820, https://doi.org/10.1016/j.jcp.2009.12.006.

[11] G. Wang, H. H. Mian, Z.-Y. Ye, J.-D. Lee, Improved point selection method for hybrid-unstructured mesh deformation using radial basis functions, AIAA Journal 53 (4) (2015) 1016–1025, https://doi.org/10.2514/1.J053304.

[12] L. Xie, H. Liu, Efficient mesh motion using radial basis functions with volume grid points reduction algorithm, Journal of Computational Physics 348 (2017) 401–415, https://doi.org/10.1016/j.jcp.2017.07.042.

[13] X. Tong, D. Thompson, Q. Arnoldus, E. Collins, E. Luke, Three-dimensional surface evolution and mesh deformation for aircraft icing applications, Journal of Aircraft 54 (3) (2017) 1047–1063, https://doi.org/10.2514/1.C033949.

[14] C. Groth, E. Costa, M. E. Biancolini, Rbf-based mesh morphing approach to perform icing simulations in the aviation sector, Aircraft Engineering and Aerospace TechnologyHttps://doi.org/10.1108/AEAT-07-2018-0178 (2019).

[15] T. D. Economon, F. Palacios, S. R. Copeland, T. W. Lukaczyk, J. J. Alonso, Su2: An open-source suite for multiphysics simulation and design, Aiaa Journal 54 (3) (2016) 828–846, https://doi.org/10.2514/1.J053813.

[16] Gori, G., and Zocca, M., and Garabelli, M., and Guardone, A., and Quaranta, G., Polimice: A simulation framework for three-dimensional ice accretion, Applied Mathematics and Computation 267 (2015) 96–107, https://doi.org/10.1016/j.amc.2015.05.081.

[17] H. Wendland, Piecewise polynomial, positive definite and compactly supported radial functions of minimal degree, Advances in computational Mathematics 4 (1) (1995) 389–396, https://doi.org/10.1007/BF02123482.

[18] G. A. Ruff, B. M. Berkowitz, Users manual for the NASA Lewis ice accretion prediction code (LEWICE), National Aeronautics and Space Administration, Lewis Research Center, Contractor Report No. 185129, Brook Park, Ohio, May, 1990.

[19] G. Gori, G. Parma, M. Zocca, A. Guardone, Local solution to the unsteady stefan problem for in-flight ice accretion modeling, Journal of Aircraft 55 (1) (2018) 251–262, https://doi.org/10.2514/1.C034412.

[20] J.-C. Tsao, S. Lee, Evaluation of icing scaling on swept NACA 0012 airfoil models, National Aeronautics and Space Administration, Contractor Report No. 217419, Glenn Research Center, Cleveland, Ohio, May, 2012, https://doi.org/10.4271/2011-38-0081.